Advanced Energy Materials

ADVANCED ENERGY MATERIALS
www.advenergymat.de

RESEARCH ARTICLE OPEN ACCESS

Breaking the Polarity–Coordination Coupling in Electrolyte Design for High-Voltage Lithium Batteries

Xue Li[1] | Shangquan Zhao[1] | Yifan Wu[1] | Naigen Zhou[1] | Fei Luo[1] | Runze Liu[1] | Chengjin Peng[1] | Junzhi Li[1] | Stefano Passerini[2,3,4] | Shan Fang[1]

[1]School of Physics and Materials Science, Nanchang University, Nanchang, Jiangxi, China | [2]Helmholtz Institute Ulm (HIU), Ulm, Germany | [3]Karlsruhe Institute of Technology (KIT), Karlsruhe, Germany | [4]International Electrochemical Energy Storage Research Institute (IEES), School of Energy Science and Engineering, Nanjing Normal University, Nanjing, China

Correspondence: Stefano Passerini (stefano.passerini@kit.edu) | Shan Fang (fangshan@ncu.edu.cn)

Received: 10 April 2026 | **Revised:** 25 June 2026 | **Accepted:** 14 July 2026

Keywords: fast-charging | high-nickel cathode | high-voltage electrolyte | solvation structure | steric hindrance

ABSTRACT

Electrolyte design is fundamentally constrained by the trade-off between high solvent polarity and weak Li^+ solvation, as polar solvents typically bind Li^+ strongly. Here, we establish a steric–electronic modulation strategy that decouples solvent polarity from Li^+ coordination, enabling a generalizable pseudo-weak solvation electrolyte design paradigm. Based on this principle, a steric hindrance–mediated electrolyte is developed combining 2,2,2-trifluoro-N, N-dimethylethylamide (DMTFA) and fluoroethylene carbonate (FEC) with dual lithium salts. Despite its strong polarity, DMTFA exhibits weak Li^+ coordination due to the combined steric hindrance and electron-withdrawing effects of the -CF_3 group, enabling anion- dominated solvation structures. This coordination chemistry lowers Li^+ desolvation barriers and drives the preferential adsorption of a B- and P-rich interphase layer at the cathode surface, thereby protecting the cathode from HF corrosion. The resulting electrolyte achieves high ionic conductivity, intrinsic flame retardancy, and an electrochemical stability window exceeding 5.0 V. Cells employing $LiNi_{0.91}Co_{0.06}Mn_{0.03}O_2$ cathodes demonstrate a capacity retention of over 90.0% after 100 cycles at 1 C rate and 4.8 V charge cut-off. The electrolyte enables approximately 1.6 Ah pouch cells to retain 84.97% capacity after 1800 cycles at 4.6 V.

1 | Introduction

The global transition toward sustainable energy systems places increasingly stringent demands on electrochemical energy storage technologies, particularly in terms of energy density, fast-charging capability, durability, and safety. Driven by carbon neutrality targets and the rapid expansion of the new energy vehicle market, high-energy lithium-ion batteries have become indispensable for transportation and grid-scale applications [1, 2]. Among various cathode materials, high-nickel content layered oxide cathodes (e.g., NCM811($LiNi_{0.8}Co_{0.1}Mn_{0.1}O_2$), NCM91 ($LiNi_{0.91}Co_{0.06}Mn_{0.03}O_2$)) have become key materials. However, when the operating voltage is raised above 4.4 V or subjected to high-rate charging, these cathodes suffer from rapid interfacial degradation, severe electrolyte oxidation, and structural instability, which collectively limit their practical deployment. In this context, the electrolyte chemistry plays a decisive role in governing interfacial reactions and ultimately determining cell performance and lifetime [3–5]. A central concept in electrolyte design is the solvation structure of Li^+, which reflects the competitive coordination between solvent molecules and anions. Because both species can act as ligands through ion–dipole or ion–ion interactions, the resulting solvation environment dictates Li^+ desolvation kinetics, interfacial charge transfer, and the chemical composition of the solid electrolyte interphase (SEI) and cathode electrolyte interphase (CEI) [6–8]. In recent years,

weakly solvating electrolytes (WSEs) have attracted considerable attention, as they favor anion-dominated solvation structures, reduce Li^+ desolvation barriers, and promote the formation of robust, inorganic-rich interphases even at moderate salt concentrations [9–12] Consequently, compared to high-concentration electrolytes [13, 14] and localized high-concentration electrolytes [15, 16], WSEs achieve a more balanced performance by simultaneously reducing viscosity and desolvation energy barriers, while preserving favorable solvation motifs associated with concentrated systems [17].

Despite these advantages, the weak solvation chemistry of WSEs is intrinsically constrained by the limited dielectric constant of the solvents employed, which inevitably restricts lithium salt solubility. In contrast, high-dielectric-constant solvents readily dissolve lithium salts but typically exhibit strong coordination with Li^+, leading to elevated desolvation barriers and sluggish interfacial kinetics. This fundamental trade-off poses a long-standing challenge: how to reconcile high salt solubility with weak Li^+–solvent interactions within a single electrolyte system. Here, we propose a mitigation through molecular design rather than solvent polarity reduction. Specifically, the introduction of bulky and electron-withdrawing substituents, e.g., the trifluoromethyl group (—CF_3), provides an effective strategy to decouple dielectric constant from Li^+ binding strength. The —CF_3 group exerts pronounced steric hindrance owing to the tetrahedral arrangement of fluorine atoms around the central carbon, which occupies substantially more space than a conventional methyl group (-CH_3) [18, 19]. Moreover, the intrinsically "lithiophobic" and strong electron-withdrawing nature of –CF_3 alters the local electronic environment, further weakening solvent and Li^+ interactions. These effects weaken solvent–Li^+ interactions even in polar molecules, thereby inducing a pseudo–weak solvation environment that retains high salt solubility.

Guided by this design principle, we develop a novel electrolyte system based 2,2,2-trifluoro-N, N-dimethylethylacetamide (DMTFA) in combination with fluoroethylene carbonate (FEC) as co-solvents to dissolve dual lithium salts (lithium hexafluorophosphate ($LiPF_6$) and lithium difluoro(oxalato)borate (LiDFOB)). Benefiting from its –CF_3-functionalized molecular structure, DMTFA simultaneously offers high polarity for efficient salt dissolution and a weakened Li^+ coordination environment, resulting in fast Li^+ desolvation kinetics. Moreover, DMTFA provides a wide electrochemical window (>5.0 V vs Li/Li^+) and high oxidative stability, making it particularly suitable for high-voltage cathodes such as NCM91. At the same time, the strong electron-withdrawing nature of the —CF_3 group in DMTFA reduces molecular reactivity, effectively suppressing parasitic oxidative decomposition at the cathode surface under high-voltage. The introduction of FEC as a co-solvent further improves interfacial solubility, while the addition of LiDFOB introduces $DFOB^-$ anions into the solvation sheath, facilitating the formation of B- and F-enriched CEI layers to protect the cathode interface from hydrogen fluoride (HF) corrosion. Collectively, this electrolyte design enables rapid Li^+ transport, mitigates lithium dendrite growth, and stabilizes electrode–electrolyte interfaces. When paired with the high-nickel cathode NCM91, the electrolyte demonstrates excellent high-voltage (up to 4.8 V) and fast-charging performance, while maintaining good capacity and long-term cycling stability even under demanding charge levels (4.5 V) and 4 C conditions. Notably, Ah-level pouch cells based on this electrolyte achieve stable operation for over 1800 cycles at 4.6 V, underscoring the practical viability of the pseudo-weakly solvating electrolyte concept.

2 | Results and Discussion

2.1 | Design of Pseudo-Weakly Solvating Structure

Density functional theory (DFT) and molecular dynamics (MD) simulations were used to study the solvation structure at the atomic scale, providing complementary theoretical insights into molecular interactions and guiding electrolyte design. Figure 1a shows the calculated energy levels of the four components in the PD14 electrolyte (1 M $LiPF_6$ + 0.1 M LiDFOB in FEC: DMTFA (1:4 v/v)). LiDFOB possesses the lowest unoccupied molecular orbital (LUMO) energy level (−1.840 eV), indicating its highest electron affinity and preferential reduction at the lithium metal surface, which promotes the formation of a robust SEI. In contrast, the highest occupied molecular orbital (HOMO) energy level of the DMTFA-Li complex decreases markedly from −7.136 to −11.885 eV upon Li^+ coordination, demonstrating enhanced oxidation stability. Benefiting from the lone-pair electrons on its carbonyl oxygen, DMTFA exhibits strong coordination capability toward Li^+. Consistently, binding energy calculations reveal a stronger Li^+ affinity of DMTFA than that of FEC, suggesting its preferential involvement in the primary solvation sheath of Li^+ (Figure 1b). MD simulations of radial distribution functions (RDF) further confirm these findings. In the absence of DMTFA (Figure 1c,e), Li ions primarily coordinate with oxygen atoms of FEC, showing a high coordination number. Although $DFOB^-$ anions participate in the first solvation sheath, their low concentration (0.1 M) limits their contribution. After adding DMTFA (Figure 1d,f), the strong Li–O(C═O) coordination occurs, combined with the high DMTFA fraction (80 vol.%) in the PD14 electrolyte ensures its dominance in the primary solvation sheath of Li ions. However, the inherent steric hindrance and electron-withdrawing effect of the —CF_3 group weakened the coordination ability of the oxygen atom, resulting in a relatively low coordination number at 3.025, and DMTFA fluorine atoms show negligible coordination with Li ions. Meanwhile, the coordination number between FEC and Li ions nearly vanishes (from 3.716 to about 0), while $DFOB^-$ anion participation increases, indicating solvation sheath reconstruction driven by DMTFA.

To investigate the DMTFA-induced solvation structure, liquid-state nuclear magnetic resonance (NMR) and Raman spectroscopy were performed on electrolytes with different compositions: pure FEC solvent, pure DMTFA solvent, PA electrolyte (1 M $LiPF_6$ in DMTFA), PFA electrolyte (1 M $LiPF_6$ in FEC: DMTFA (1:4 v/v)), PD14 electrolyte, and PD15 electrolyte (1 M $LiPF_6$+0.1 M LiDFOB in FEC: DMTFA (1:5 v/v)). As shown in Figure S1 and Figure 1g, the Raman spectra revealed characteristic vibrational modes in different regions: the 400–800 cm^{-1} region primarily corresponds to inorganic salts ($LiPF_6$, LiDFOB), with P-F symmetric stretching vibration peaks appearing near 700–750 cm^{-1} and B-F vibration peaks near 500–600 cm^{-1} [20, 21]. Organic solvent bonds such as C-O and C-F may appear in the 800–1600 cm^{-1} range [22]. In the PA system, where DMTFA serves as the single solvent, strong peaks were observed for

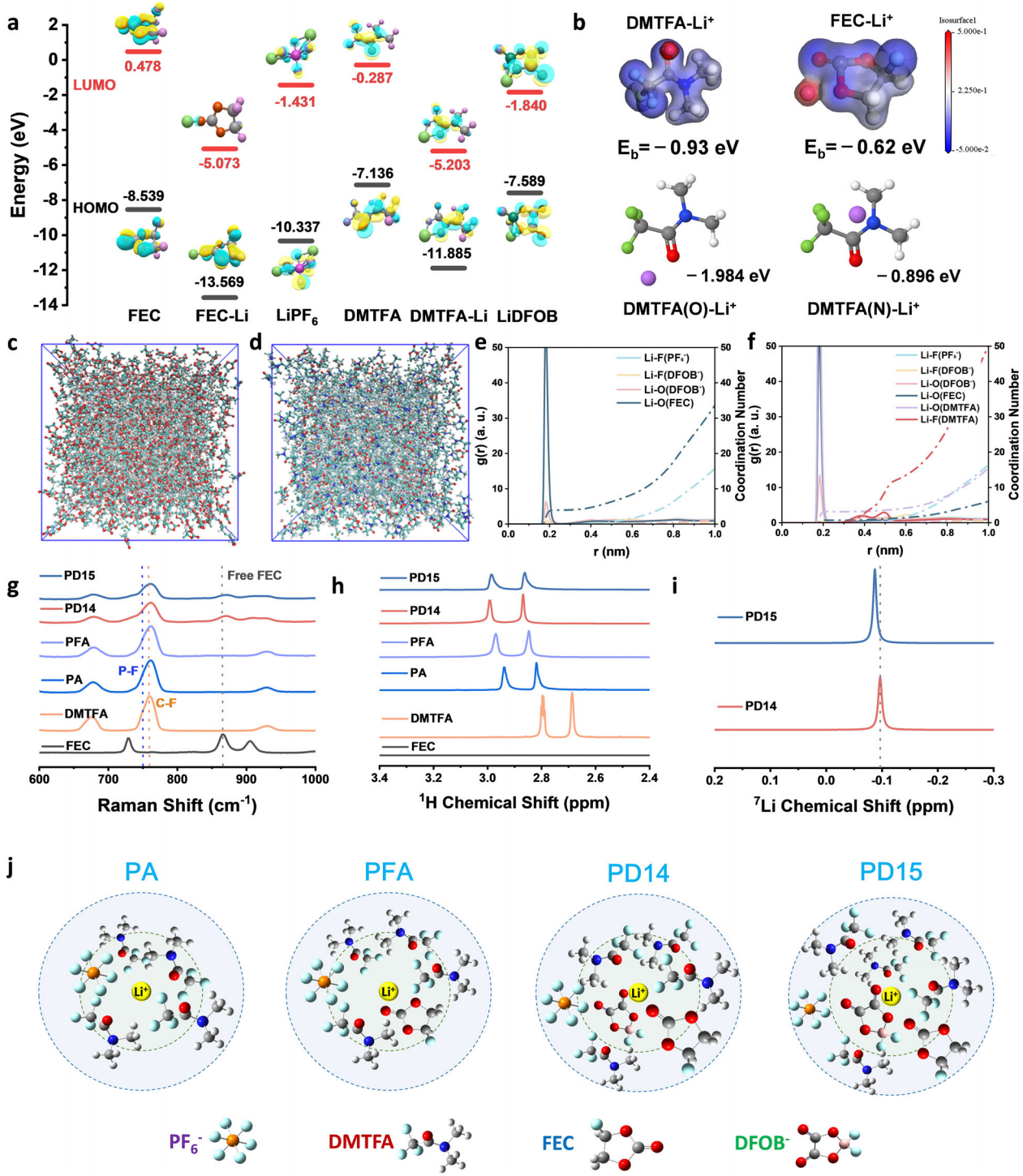

FIGURE 1 | (a) LUMO-HOMO energy levels and (b) binding energies with lithium ions for various solvents. MD simulation snapshots and RDFs for (c,e) electrolyte without DMTFA and (d,f) PD14 electrolyte. (g) Local Raman spectra, (h) ^{1}H NMR, and (i) ^{7}Li NMR spectra for different solvents and electrolytes. (j) Schematic illustration of the solvation structures in different electrolytes.

C═O (~1700 cm^{-1}), CH_3 (~1425 cm^{-1}), and C-F (~760 cm^{-1}), while the P-F peak of PF_6^- (~750 cm^{-1}) appeared weak or overlapped with DMTFA peaks. This suggests either incomplete dissolution of $LiPF_6$ or weak interaction with DMTFA, indicating Li^+ may preferentially coordinate with the C═O group of DMTFA. However, the strong shielding effect of DMTFA likely limits Li^+ contact with PF_6^-, masking the PF_6^- signal. When FEC was introduced (PFA system), the overall spectral pattern remained largely unchanged, while the C═O peak intensity slightly decreased, possibly due to competition between FEC and DMTFA for Li^+ coordination. In PD14, the addition of $DFOB^-$ weakened the P-F peak of PF_6^- through competitive coordination, forming more stable coordination structures with Li^+ (e.g., [Li^+-$DFOB^-$]) complexes that stabilize Li^+ solvation and suppress PF_6^-/FEC decomposition. To further demonstrate the strong coordination between $DFOB^-$ and Li^+, solvation structures with and without

LiDFOB were constructed, respectively. As shown in Figure S2, RDF calculations reveal that upon the addition of a small amount of $DFOB^-$, the coordination number of PF_6^- slightly decreases, while that of $DFOB^-$ is slightly higher than that of PF_6^-. This indicates that $DFOB^-$ can preferentially form a stable coordination with Li^+ and partially replace PF_6^- in the solvation sheath of the electrolyte. Furthermore, the solvation sheath binding energy shows that the binding energy of the sheath containing $DFOB^-$ is more negative than that without $DFOB^-$, suggesting that $DFOB^-$ is more prone to participate in the solvation structure compared to PF_6^-. The appearance of free FEC peaks at 868 and 1825 cm^{-1} confirms this competition, consistent with RDF results. In the PD15 system with additional DMTFA, the P-F peak of PF_6^- further weakened, forming a DMTFA-dominated solvation sheath that actually limits PF_6^- dissociation. Notably, free DMTFA peaks remained prominent in all four electrolyte systems (PA, PFA, PD14, PD15), demonstrating that in the solvation sheath, the three F atoms of $-CF_3$ create a steric barrier around the carbonyl oxygen, hindering Li^+ access to its lone pair electrons, while their electron-withdrawing effect reduces the electron cloud density of the oxygen atom. This results in minimal Li^+ coordination by DMTFA, establishing a solvation structure typical of a pseudo–weak solvation environment.

NMR analysis further substantiates these conclusions. In the PA system, the ^1H NMR (Figure S3a, Figure 1h) shows the proton signal of the $N(CH_3)_2$ group in neat DMTFA located at approximately 2.68-2.80 ppm. When DMTFA serves as the sole solvent in the presence of $LiPF_6$ (PA system), this signal distinctly shifts downfield to approximately 2.82-2.95 ppm, indicating a significant coordination interaction between Li^+ and DMTFA. The coordination of Li^+ with the carbonyl oxygen redistributes the electron density of the amide group through an inductive effect, reducing the shielding effect around the protons of the $N(CH_3)_2$ group, which consequently gives rise to a downfield shift of the ^1H signal [23]. Upon the introduction of FEC, the proton signal of DMTFA shifts further downfield, indicating that the addition of FEC alters the local coordination environment around Li^+, with both FEC and DMTFA jointly participating in the construction of the Li^+ solvation structure, thereby further modulating the electronic environment of DMTFA. In the PD14 system, the -CH_3 signal continues to shift downfield, suggesting that the introduction of $DFOB^-$ further reconstructs the primary Li^+ solvation sheath. Combined with Raman spectroscopy and MD simulation results, it can be inferred that $DFOB^-$ partially enters the primary solvation sheath and participates in Li^+ coordination, thereby altering the electronic environment of the DMTFA molecules involved in coordination. When the DMTFA proportion is further increased to PD15, the -CH_3 signal shifts slightly upfield compared to that of PD14, indicating that the average Li^+-DMTFA interaction experienced by DMTFA molecules is somewhat weakened, which is consistent with the formation of a more rigid DMTFA-enriched solvation structure constructed by an excessive amount of DMTFA. In the ^{19}F NMR (Figure S3b, c), the -CF peak signal of FEC appears at −123 ppm, while while neat DMTFA exhibits a prominent $-CF_3$ singlet signal at −70.6 ppm. Upon the addition of $LiPF_6$, new weak peaks emerge at −72.9 ppm and −74.8 ppm. However, it is noteworthy that the main $-CF_3$ peak of DMTFA shifts only slightly from −70.6 ppm to −70.3 ppm, showing virtually no significant chemical shift variation. This indicates that the $-CF_3$ group is only weakly affected by Li^+ coordination. The absence of appreciable chemical-shift changes across different electrolyte formulations further confirms that DMTFA undergoes no detectable decomposition, consistent with the Raman spectroscopy and MD simulation results. This is consistent with the results of Raman and MD data. In the NMR ^7Li spectrum (Figure 1i), the signal peak shifts downfield from PD14 to PD15, indicating stronger Li^+–solvent coordination and reduced anionic participation with increasing DMTFA content [24].

Based on the above data analysis, schematic illustrations of the solvation structures for the four electrolytes are presented in Figure 1j. It can be concluded that DMTFA dominates the primary solvation sheath of Li^+ in the PA system. In the PA system, $LiPF_6$ exhibits limited dissociation, with PF_6^- existing mainly as contact ion pairs, constraining ionic conductivity. After the introduction of FEC (PFA system), the C-O groups of FEC form competitive coordination with Li^+, partially replacing DMTFA and forming a mixed solvation sheath. The addition of FEC dilutes the concentration of DMTFA, weakens its coordination effect, while the high-dielectric environment provides strong electrostatic screening that disrupts contact ion pairs and liberates anions, thereby improving the ionic conductivity. Meanwhile, the fluorine-containing characteristics of FEC contribute to the formation of a stable SEI film enriched with LiF. The addition of LiDFOB (PD14 system) introduces $DFOB^-$ anions, which strongly chelate Li^+ ions via their carbonyl oxygen atoms, forming stable complexes like [Li^+-$DFOB^-$]. This reconstructs the primary solvation sheath and preferentially directs the decomposition of $DFOB^-$ during SEI/CEI formation. This preferential reduction suppresses the detrimental decomposition of PF_6^-, leading to a more stable and functional interphase. In PD15, the excessively high DMTFA fraction leads to a DMTFA-dominated and relatively rigid solvation structure. The over-enrichment of DMTFA in the primary solvation sheath weakens the synergistic solvation effect between FEC and DMTFA, increases the proportion of tightly bound ion pairs and aggregates. Consequently, Li^+ transport is hindered, resulting in a decreased ionic conductivity. The "pseudo-weakly solvating" characteristic of PD14 does not pursue extreme "weak coordination." Instead, it skillfully leverages steric and electron-withdrawing effects to modulate reaction kinetics and employs preferential coordination by the functional anion ($DFOB^-$) to guide favorable interfacial reactions without significantly compromising ion transport rates. Consequently, this design achieves precise regulation of a clever solvation structure that balances polar solvent molecules with weak Li^+ coordination, while maintaining relatively high ionic conductivity.

2.2 | Electrolyte Physical Properties and Compatibility With Lithium Anode

The use of DMTFA solvent successfully established an effective "pseudo-weakly solvating" environment. Benefiting from its inherent strong polarity, the Li^+ transport kinetics of the entire electrolyte system were also enhanced. Contact-angle tests (see Figure 2a,b) reveal that PD14 exhibits significantly improved wettability compared to the system without DMTFA, with its contact angle reduced by nearly half. This clearly demonstrates that

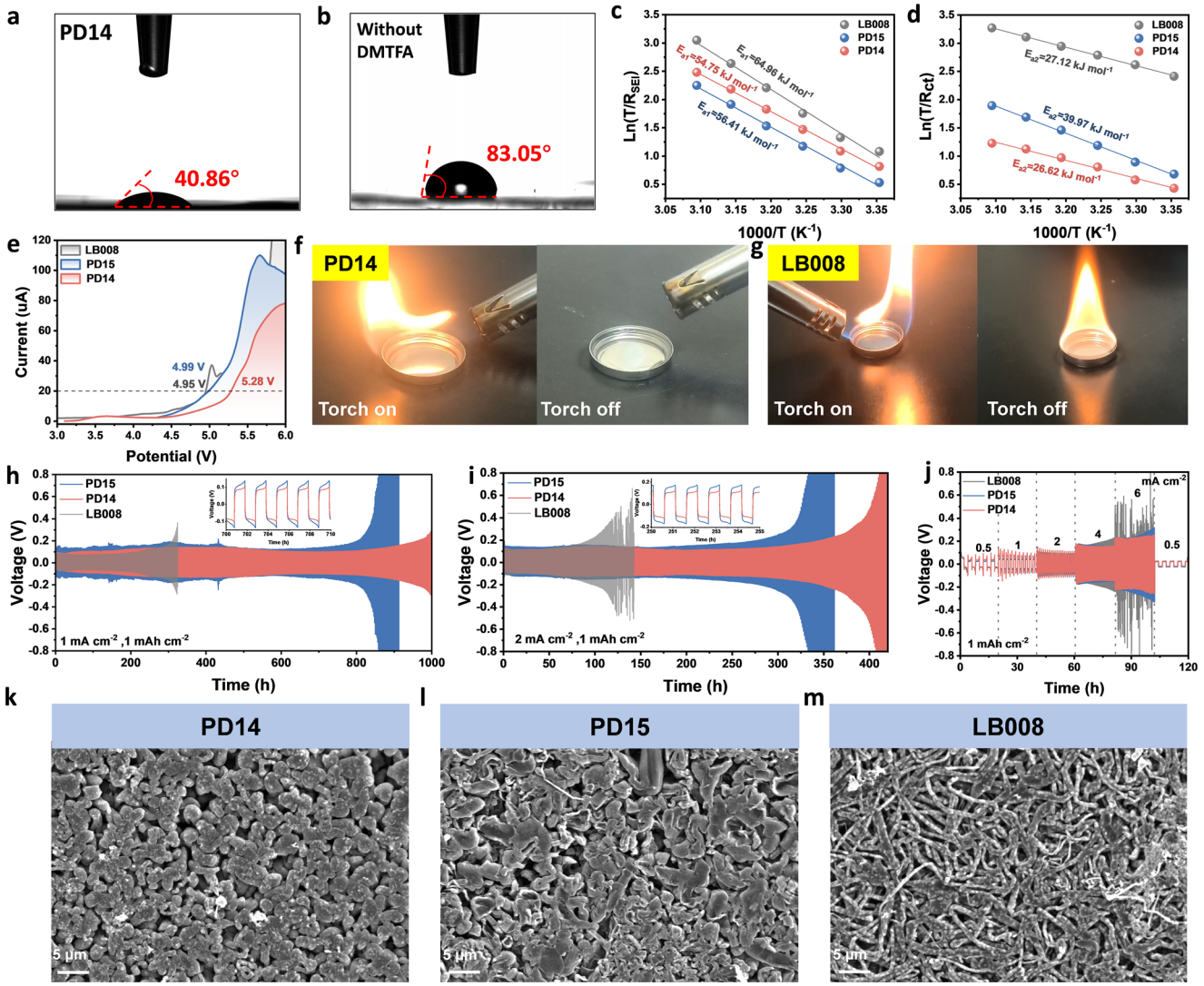

FIGURE 2 | Contact-angle test for (a) PD14 and (b) the PD14 electrolyte without DMTFA. Activation energy barrier for (c) Li^+ transport through the SEI and (d) Li^+ desolvation. (e) Electrochemical window of the three electrolytes; ignition test of (f) PD14 and (g) LB008 electrolytes. Cycling performance of Li||Li symmetric cells at 1 mAh cm^{-2} under (h) 1 mA cm^{-2}, (i) 2 mA cm^{-2} and (j) various current densities (see values in the figure). (k–m) SEM images of lithium metal surface after first-cycle deposition in PD14, PD15 and LB008.

DMTFA incorporation effectively improves electrolyte wetting ability. Furthermore, Figure S4 presents the difference in wetting behavior between FEC and DMTFA. Owing to the rapid spreading and instantaneous infiltration of neat DMTFA, its contact angle could not be accurately determined; in contrast, neat FEC exhibits a contact angle of 52.32°. As DMTFA is added, the contact angle of PD15 decreases to 31.60°, which is smaller than that of PD14, indicating that a higher proportion of DMTFA can further enhance the wetting performance of the electrolyte. Activation energy barriers for Li^+ transport and desolvation within the SEI are critical parameters to evaluating electrolyte performance. Lowering these barriers enhances Li^+ transport efficiency, reduces polarization, mitigates lithium dendrite growth risks, and improves interfacial stability, thereby extending battery cycle life [25, 26]. To quantify ion transport dynamics, electrochemical impedance spectroscopy (EIS) was conducted on Li||Li symmetric cells within 25°C and 50°C (Figure S5), and the activation energy was extracted by Arrhenius fitting (Figure 2c,d). PD14 electrolyte exhibited the lowest activation energy barrier for Li^+ transport through the SEI (E_{a1}) and activation energy barrier for Li^+ desolvation (E_{a2}), facilitating rapid ionic transport and improving rate performance. The ionic conductivities of various formulations were then evaluated at room temperature. As shown in Figure S6, all PD-series electrolytes exhibit higher conductivity than the commercial LB008 electrolyte. At 30°C, PD14 records 9.13 mS cm^{-1}, whereas PD15, owing to limited lithium-salt dissociation, reaches 8.97 mS cm^{-1}; commercial LB008 gives 7.42 mS cm^{-1}. In addition, the lithium-ion transference number (t_{Li^+}) of the various electrolytes are presented in Figure S7. The t_{Li^+} values for PD14, PD15, and LB008 are 0.59, 0.47, and 0.43, respectively. PD14 simultaneously exhibits relatively high ionic conductivity and the highest Li^+ transference number among the three systems, indicating that the solvation environment constructed by the synergy of high polarity and steric hindrance can facilitate efficient Li^+ transport and enhance its contribution to the total ionic conduction. This is beneficial for mitigating concentration polarization, thereby laying the foundation for the superior rate capability and cycling stability observed in subsequent tests.

The electrochemical stability window of the PD-series electrolytes was investigated using linear sweep voltammetry (LSV) to assess their high-voltage applicability. As shown in Figure 2e, the PD-series electrolytes exceed 4.9 V, with PD14 even reaching up to 5.28 V, indicating that the PD-series electrolytes possess superior oxidation resistance, fully meeting the operational requirements for high-voltage lithium batteries. Safety performance is another critical metric for electrolyte design, thus, flame tests were conducted as illustrated in Figure 2f,g. The results show that PD14 exhibits excellent flame-retardant properties, remaining non-flammable even under continuous ignition. In contrast, the commercial LB008 electrolyte continued to burn after the ignition source was removed. These results confirm that PD14 may greatly enhance the safety performance of batteries, effectively addressing the flammability issue of conventional organic electrolytes.

The interfacial compatibility of PD electrolytes with lithium metal was evaluated using Li||Li symmetric cells cycled at current densities of 1, 2, and 4 mA cm^{-2}. As shown in Figure 2h, under the 1 mA cm^{-2} condition, PD14 exhibited stable cycling for 1000 h while maintaining a steady polarization voltage. PD15 also sustained over 800 h of cycling before showing an increase in polarization voltage. Even at higher current densities of 2 and 4 mA cm^{-2} (Figure 2i and Figure S8), the PD-series electrolytes still demonstrated stable cycling for over 300 and 100 h, respectively. In contrast, the cell with LB008 electrolyte experienced a rapid rise in polarization voltage and early failure, likely caused by lithium dendrites piercing the separator.

Remarkably, even at a high current density of 6 mA cm^{-2}, Li||Li cells employing PD14 and PD15 electrolytes maintained low polarization voltages and stable cycling. Moreover, when the current density was reduced to 0.5 mA cm^{-2}, the cells continued to demonstrate excellent cycling performance. In contrast, the LB008 electrolyte-based cell failed rapidly under 6 mA cm^{-2} (Figure 2j). These results indicate that the PD-series electrolytes exhibit superior compatibility with lithium metal anodes, effectively suppressing lithium dendrite formation and preventing interfacial degradation. The EIS results (Figure S9) further confirmed that the interfacial impedance of PD14 significantly decreased with cycling, ultimately stabilizing at a much lower value than LB008 after 100 cycles. However, excessive DMTFA (PD15) led to the electrolyte impedance increase (high frequency intercept) after prolonged cycling. To further quantitatively evaluate the reversibility of lithium plating/stripping in different electrolytes, the Aurbach method was employed to measure the Coulombic efficiency (CE) of Li||Cu cells. As shown in Figure S10, PD14 delivers a high average CE of 98.90%, while PD15 exhibits a slightly lower value of 98.61%, both of which are significantly superior to that of the LB008 system (88.21%). These results indicate that both PD14 and PD15 can effectively suppress the formation of "dead lithium" and parasitic side reactions, thereby achieving significantly enhanced reversibility of lithium plating/stripping.

To better understand lithium deposition behavior on lithium anodes under different electrolytes, scanning electron microscopy (SEM) was performed on Li||Li symmetric cells after the first cycle. As shown in Figure 2k–m, PD-series electrolytes exhibited a dense, block-like lithium deposits without noticeable lithium dendrite formation. PD14 in particular yielded compact and uniform deposits, indicating uniform diffusion and reduction of lithium ions on the electrode surface. In contrast, the cell with LB008 showed extensive filamentary lithium dendrites, explaining their rapid failure. In situ optical microscopy (Figure S11) corroborated these findings: LB008 led to uneven and dendritic deposition over time, while PD14 enabled uniform and dense deposition forming a thin, continuous layer. Both SEM and in situ optical microscopy confirm that PD-series electrolytes effectively suppress lithium dendrite growth, reducing the risk of separator penetration, and markedly improve overall cell safety and stability.

2.3 | High-Voltage and Fast-Charging Cycling Performance of NCM91

To investigate the compatibility between PD14 and high-nickel cathodes, Li||NCM91 cells were assembled for testing. As shown in Figure 3a, at a cutoff voltage of 4.3 V, PD14 enabled highly stable cycling for 1000 cycles, delivering a discharge specific capacity of 125.32 mAh g^{-1}, corresponding to a capacity retention of 73.94%. The PD15 electrolyte, with a higher DMTFA content, also demonstrated good cycling stability, achieving 68.19% capacity retention after 800 cycles. In sharp contrast, the commercial LB008 electrolyte-based cell exhibited severe capacity degradation after only 250 cycles. The electrolyte without DMTFA (designated as PDF: 1 M $LiPF_6$ + 0.1 M LiDFOB-FEC) failed to support cycling in Li||NCM91 cells due to excessively high impedance (Figure S12). To further probe high-voltage durability, cycling was examined at cutoff voltages of 4.5, 4.6, and 4.7 V. At 4.5 V (Figure 3b and Figure S13), PD14 supported stable cycling for 500 cycles with 78.55% capacity retention, while PD15 showed inferior performance compared to PD14, i.e., 86.51% vs 91.98% after 300 cycles. The corresponding charge/discharge curves are shown in Figure S13. Under more challenging conditions of 4.6 and 4.7 V, PD14 demonstrated superior performance, maintaining 81.26% and 84.50% capacity retention after 300 cycles, respectively (Figure S14). The highest capacity retention at 4.7 V infers for a more performing CEI established at such high voltage. In contrast, as shown in Figure S15, both the PA and PFA control electrolytes exhibit significant capacity decay at a cutoff voltage of 4.7 V. To verify the rationality of the solvent composition in PD14, we reduced the DMTFA volume fraction to formulate the PD13 electrolyte for comparison. The results show that PD13 achieves a capacity retention of only 57.03% after 300 cycles, which is significantly lower than that of PD14, indicating that the solvent composition adopted in PD14 is more favorable for achieving stable high-voltage cycling performance.

Interestingly, the DMTFA single-solvent electrolyte (11PD: 1 M $LiPF_6$ + 0.1 M LiDFOB in DMTFA) also demonstrated an electrochemical window exceeding 5 V and maintained normal charge/discharge behavior at a 4.8 V/1 C condition, although its cycling retention remained insufficient (Figure S16). In contrast, cells using PD14 electrolyte with FEC co-solvent exhibited stable cycling for 100 cycles while maintaining over 90% capacity retention (Figure 3c). The LB008 electrolyte showed inferior performance with only 82.81% capacity retention (Figure 3c), with corresponding charge/discharge curves presented in Figure 3d,e. EIS (Figure 3f, g) revealed that PD14 electrolyte

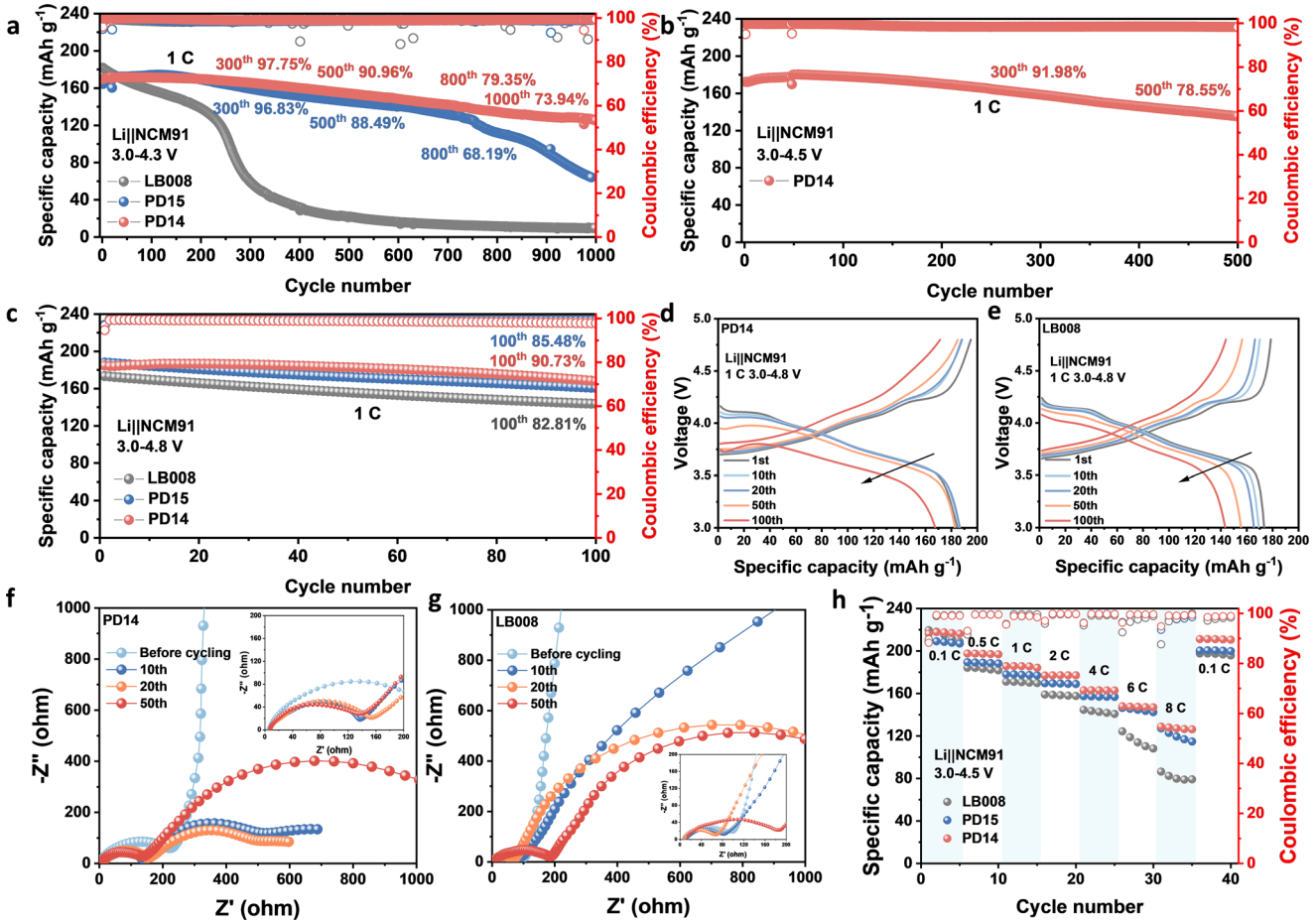

FIGURE 3 | Electrochemical performance of Li||NCM91 cells with different electrolytes at 1 C: (a) at 4.3 V, (b) at 4.5 V, (c) at 4.8 V, with corresponding (d,e) selected charge–discharge curves and (f,g) EIS. (h) Rate capability from 0.1 C to 8 C at 4.5 V.

exhibited continuously decreasing impedance during cycling, attributable to superior interfacial film formation that facilitated ion transport. After 50 cycles, its impedance became significantly lower than LB008. Compared to other electrolytes, PD14 offered outstanding cycling stability at high cutoff voltages, indicating effective suppression structural degradation of the Ni-rich cathode. Rate capability tests at 4.5 V under 0.1 C–8 C rates (Figure 3h) showed that PD14 enabled approximately 140 mAh g^{-1} specific capacity even at 8 C rate, with high-capacity recovery when returning to 0.1 C. Conversely, LB008 electrolyte exhibited significant capacity fading above 6 C, delivering less than 100 mAh g^{-1} at 8 C rate.

Considering the demand for fast-charging devices, the cycling performance of PD14 was evaluated at 4.5 V cutoff voltage under high rates of 2 C and 4 C (Figure 4a, b). The results show as PD14 maintained 89.94% capacity retention after 500 cycles at 2 C rate, and over 70% capacity retention even at the ultra-high 4 C rate, demonstrating outstanding fast charge/discharge cycling performance. To demonstrate the superior reversibility of lithium anodes with PD14, full-cell tests were performed with 50 μm-thin lithium anodes (Figure 4c). At 4.5 V charge cut-off voltage, the cell maintained 87% capacity retention after 350 cycles, while cells with LB008 suffered abrupt capacity decay after 170 cycles, delivering less than 20 mAh g^{-1} by 350 cycles. This confirms PD14 to form a highly stable SEI, effectively suppressing continuous electrolyte decomposition and lithium corrosion while promoting uniform lithium plating.

Differential capacity (dQ/dV) curves provide insights on the electrochemical reactions by showing voltage derivatives of charge quantity [27]. For LB008, peak shifts toward lower potentials and significant attenuation occurred during cycling, nearly vanishing after 300 cycles, indicating severe polarization, lithium depletion, and irreversible H2-H3 phase transitions corresponding to capacity loss [28, 29]. In contrast, PD14-based cells showed minimal peak shift in the first 100 cycles and only minor shift by 300 cycles, indicating a suppressed structural collapse of the cathode (Figure 4d,e). Pouch cell testing provides more practical evaluation of electrolyte performance. The PD14 electrolyte was introduced into approximately 1.6 Ah Graphite||NCM91 pouch cells (N/P = 1.1), which were cycled at 4.6 V, as shown in Figure 4f,g. The pouch cells demonstrated extended cycle life under high-voltage conditions, achieving an exceptional capacity retention of 84.97% after 1800 cycles with an average Coulombic efficiency near 100%. This directly proves that the PD14 electrolyte designed in this experiment is inherently compatible with the NCM91 cathode. It also demonstrates the electrolyte's versatility: it can stabilize highly reactive lithium metal anodes, support high-voltage cathodes, and maintain the performance of traditional graphite anodes without compromise. Combined with the stable cycling results of high-capacity pouch cells, these

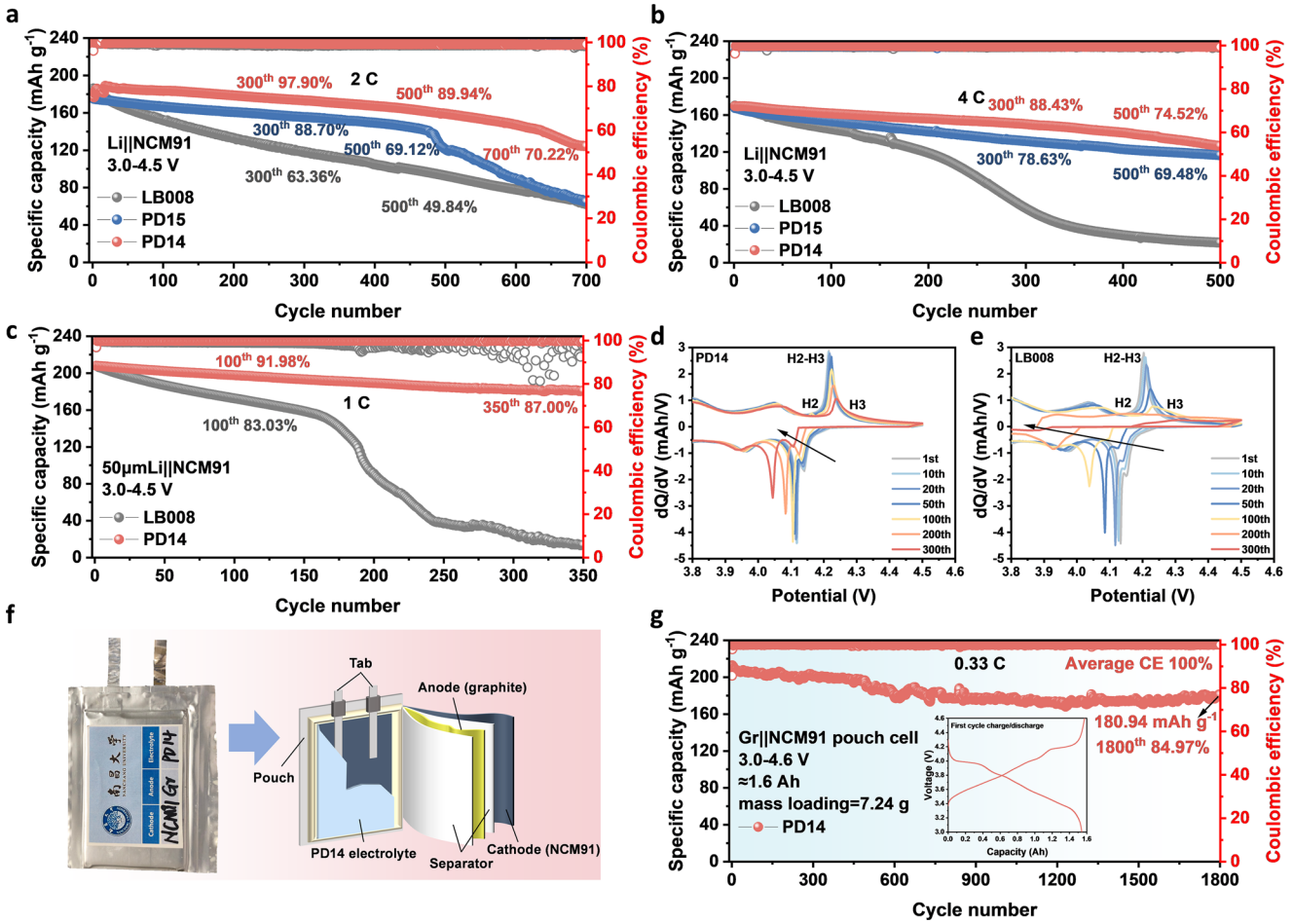

FIGURE 4 | Electrochemical performance of Li||NCM91 cells evaluated at 4.5 V: (a) cycling stability at 2 C and (b) at 4 C. (c) Cycling performance of 50 μm Li||NCM91 cells with (d,e) corresponding selected dQ/dV curves. (f,g) Structure and 4.6 V cycling performance of Gr||NCM91 pouch cells.

findings collectively demonstrate the strong potential of PD14 for next-generation high-energy-density battery systems.

2.4 | Cathode Interface Morphology and Composition

The NCM ternary cathode undergoes irreversible structural degradation during cycling in lithium metal batteries, which is a major factor contributing to capacity decay. The significant lattice mismatch between the layered bulk structure and surface rock-salt phase generates high interfacial lattice strain, ultimately leading to irreversible structural deterioration through bulk fatigue under high-voltage cycling [30]. Consequently, chemo-mechanical cracking is frequently observed in cycled Ni-rich cathode particles, which is believed to accelerate side reactions with the electrolyte and promote the formation of a thick and low ionic conductivity CEI layer [31, 32]. As shown in Figure 5a–c, after 500 cycles at 4.5 V and 2 C, cathodes cycled in PD14 electrolyte maintained intact secondary particles with tightly interconnected primary particles. In contrast, those cycled in PD15 exhibited minor microcracks, while those in LB008 showed severe cracking of secondary particles, correlating with pronounced capacity decay. Cross-sectional SEM images of NCM91 cathodes further confirmed these trends. After 500 cycles, PD14-electrolyte cells displayed only slight microcracks, whereas control samples exhibited pronounced internal fracturing (Figure S17). Similarly, post-cycling morphology at 4.8 V after 100 cycles (Figure S18) demonstrated severe particle fragmentation in LB008, while PD14-preserved particles retained structural integrity. This superior cathode stability correlates with the exceptional high-voltage performance of PD14.

In lithium batteries, the NCM cathode material undergoes structural transformations during charge/discharge cycles, particularly under high-voltage or high-temperature conditions. Transition metal ions may migrate from their original sites into lithium layers, causing structural instability. This migration is often accompanied by oxygen vacancy formation, as transition metal ions may carry away oxygen atoms during displacement, or oxygen deficiency may facilitate metal ion movement. Such structural changes favor the collapse of the R-3m layered structure to spinel (e.g., $LiNi_2O_4$) or rock-salt phases (e.g., NiO) [33]. These transformations negatively impact battery performance, manifesting as capacity fade and voltage decay. To elucidate how different electrolytes affect surface reconstruction and CEI development, high-resolution transmission electron microscopy (HRTEM) was employed to examine CEI morphology after 100 cycles at 4.8 V (Figure 5d,f). The PD14 electrolyte formed an ultrathin (4.68 nm), smooth, and uniform CEI layer, while the

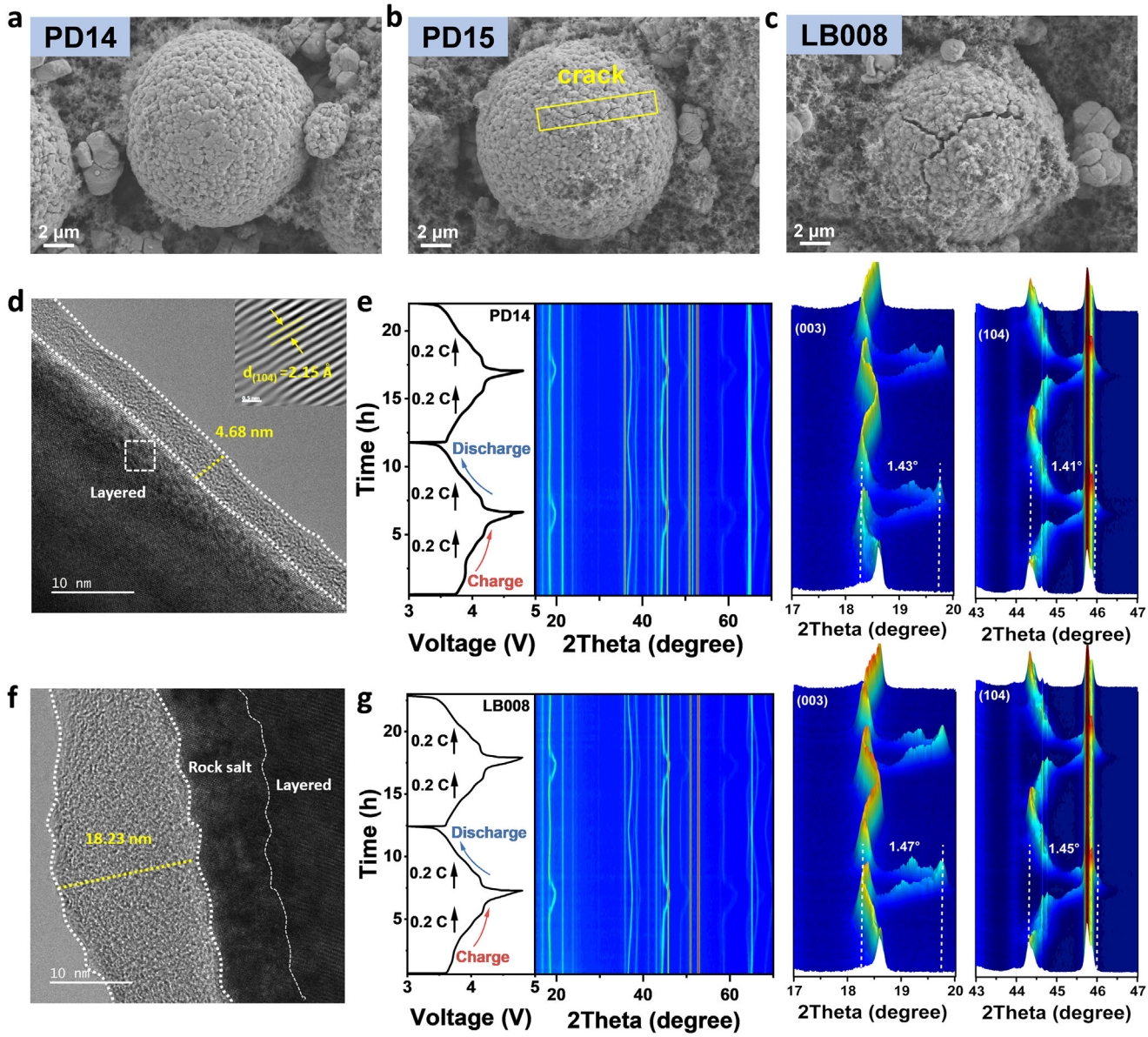

FIGURE 5 | Li||NCM91 cell analysis: (a–c) SEM of cathodes after 500 cycles at 4.5 V/2C in the three electrolytes. TEM and in situ XRD of a cathode cycled at 4.8 V in (d, e) PD14 and (f, g) LB008.

cathode maintaining distinct layered structure characteristics. In stark contrast, LB008 produced a CEI layer approximately 18.23 nm thick (four times thicker than PD14) with irregular protrusions, accompanied by pronounced rock-salt phase formation in the active material—evidence of irreversible phase transitions. Similar observations were made for NCM91 cathodes after 300 cycles at 4.3 V (Figure S19). The PD14 electrolyte again generated a thinner CEI (8.25 nm) and well-preserved lattice.

In situ X-ray diffraction (XRD) further corroborated the superior structural stability imparted by PD14. Cells containing the two electrolytes were cycled at 4.8 V under 0.2 C for 2 cycles to monitor lattice parameter evolution. As shown in Figure 5e,g, the NCM91 cathode underwent sequential phase transitions during charge/discharge: from hexagonal H1 phase to monoclinic M phase, then to hexagonal H2 phase, and finally to hexagonal H3 phase. During the initial charging stage, the (003) peak first shifted toward lower 2θ angles and then to higher angles, indicating significant *c*-axis lattice contraction during the H2-H3 phase transition. When charged to 4.8 V, the maximum peak shift in PD14 was 1.43°, smaller than the shift of LB008 (1.47°). Similar trends were also observed for the (104) reflection. These results confirm that PD14 effectively suppresses excessive *c*-axis contraction and mitigates irreversible lattice deformation, thereby enhancing structural resilience during high-voltage cycling [34, 35].

To further investigate and compare the composition of the CEI formed in various electrolytes, X-ray photoelectron spectroscopy (XPS) was performed on cathodes cycled in PD14 and LB008. According to the XPS elemental analysis results in Figure S20, the LB008 control group exhibited a significantly higher percentage of organic-related elements (C and O), while in contrast, the

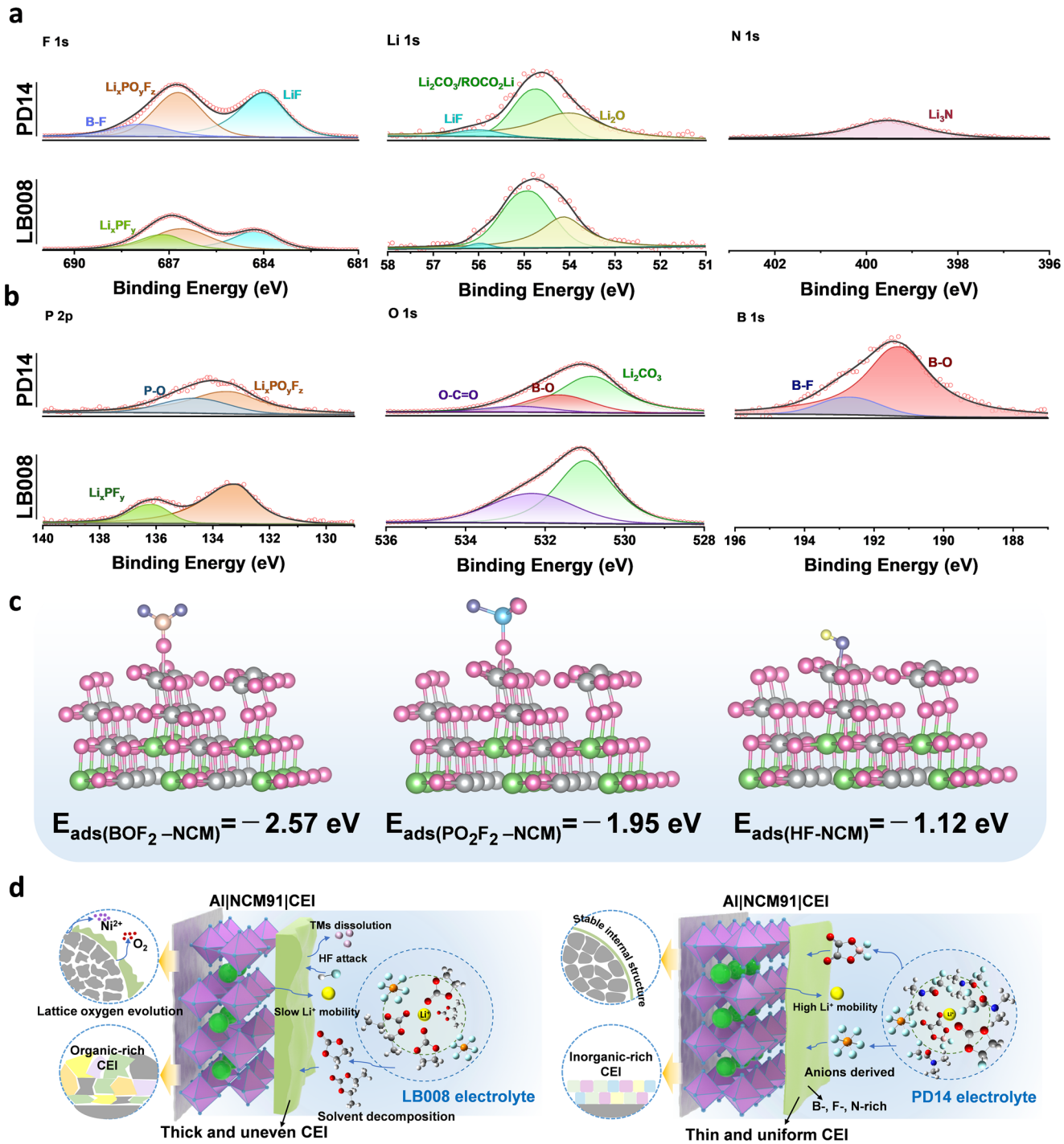

FIGURE 6 | XPS spectra of NCM91 cathode after 100 cycles at 4.8 V/1C: (a) F 1s, Li 1s, N 1s, (b) P 2p, O 1s, and B 1s. (c) Calculation of adsorption energies for various species on the NCM interface. (d) Schematic illustration of the interfacial mechanisms of LB008 and PD14 electrolytes at the cathode.

PD14 experimental group showed a more prominent proportion of the F element, which represents inorganic components. As shown in Figure 6a,b, the F 1s and Li 1s spectra revealed higher LiF inorganic content in the CEI of the PD14-cycled cathode, which significantly enhances mechanical strength and chemical inertness. Meanwhile, due to its electronic insulating nature (with a bandgap of approximately 14.6 eV), LiF blocks electron tunneling and prevents continuous decomposition of the electrolyte [36]. Additionally, B-F species were detected in the CEI of the cathode tested in PD14. The P 2p and O 1s spectra showed distinct P-O and B-O components on the PD14 cathode compared to LB008, with B-F and B-O bonds corresponding to features in the B 1s spectrum. These boron-based compounds form a uniform interfacial film that suppresses electrolyte oxidative decomposition and reduces the generation of gases such as CO_2 and O_2 [37, 38]. The presence of P-O species helps delay cathode structural collapse, inhibits layered-to-spinel phase transitions, and stabilizes high-voltage performance of the cell. Simultaneously, both components can preferentially adsorb onto the cathode surface, thereby preventing corrosive attack

from residual HF in the electrolyte on the cathode material [39]. As shown in Figure 6c, the adsorption energies of PF_6^- and $DFOB^-$ decomposition products ($PO_2F_2^-$ and BOF_2^-) as well as HF on the NCM91 cathode interface were calculated, respectively. The results show that the adsorption energies of both $PO_2F_2^-$ and BOF_2^- on the NCM91 surface are more negative than that of HF, indicating that these decomposition products have stronger affinity to the cathode interface. They preferentially bind to and passivate the cathode surface, protecting it from HF attack. Meanwhile, in situ differential electrochemical mass spectrometry (DEMS) results confirmed (Figure S21) that during the charging of Li||NCM91 cells to 4.8 V, the cell with PD14 electrolyte generated a significantly lower amount of HF gas compared to the LB008 electrolyte. This indicates that PD14 can effectively suppress HF generation. Furthermore, Li_3N was identified in the N 1s spectrum due to the $N(CH_3)_2$ group in DMTFA, with its ultrahigh Li^+ conductivity ($\sim 10^{-3}$ S cm^{-1}) significantly reducing cathode/electrolyte interfacial resistance and improving rate capability [40, 41]. These beneficial components were also detected on cathodes cycled at 4.3 V/1 C (Figure S22), further confirming the advantageous interfacial decomposition of PD14 electrolyte anions.

The reaction mechanisms for cells with PD14 and LB008 electrolytes are shown in Figure 6d. In PD14, the $-CF_3$ group's steric hindrance and electron-withdrawing effect promote weak DMTFA-Li^+ coordination. This drives anions (PF_6^-/$DFOB^-$) to decompose preferentially at the interface, forming a thin, uniform, and inorganic-rich CEI layer on the NCM91 cathode. This design effectively suppresses transition metal dissolution and irreversible phase changes in the high-nickel cathode, mitigating structural damage and providing a key foundation for a stable system. In contrast, commercial LB008 electrolyte lacks such solvation control. Its interface is governed by disordered solvent decomposition, leading to a thick, uneven, and organic-heavy CEI layer that offers poor protection. This disordered interfacial evolution fundamentally explains its inferior cycling stability compared to PD14.

3 | Conclusions

This work establishes a transferable electrolyte design paradigm in which Li^+ coordination strength is decoupled from solvent polarity through synergistic steric–electronic regulation. By employing a strongly polar yet sterically hindered solvent, DMTFA, the Li^+ solvation environment is fundamentally reconfigured: although DMTFA participates in the solvation sheath, its $-CF_3-$induced steric hindrance and electron-withdrawing effects suppress direct Li^+ coordination and shift the solvation equilibrium toward FEC and PF_6^-/$DFOB^-$ anions. This tailored coordination chemistry drives preferential anion-derived interfacial reactions, leading to the in situ formation of a dense, inorganic-rich composite interphase dominated by LiF and distinctive B–F, B–O, P–O, and Li_3N species. As a result, continuous electrolyte oxidation, transition-metal dissolution, and interfacial parasitic reactions are effectively suppressed, enabling stable Li||NCM91 cycling up to 4.8 V, sustained fast-charging operation (4.5 V, 2 C/4 C) for over 500 cycles, and an 84.97% capacity retention after 1800 cycles in a ~1.6 Ah pouch cell at 4.6 V. Beyond this specific system, our results demonstrate that steric and electronic molecular engineering provides a powerful route to rationally design high-performance electrolytes for high-energy, high-voltage lithium batteries.

Author Contributions

Xue Li: methodology, formal analysis, investigation, Writing – original draft. **Chengjin Peng**: formal analysis, validation. **Shan Fang**: supervision, resources, project administration, funding acquisition, conceptualization. **Shangquan Zhao**: formal analysis, software. **Stefano Passerini**: conceptualization, supervision, writing – review and editing. **Fei Luo**: formal analysis, validation. **Yifan Wu**: software, formal analysis. **Naigen Zhou**: writing – review and editing, resources. **Runze Liu**: formal analysis, writing – review and editing. **Junzhi Li**: formal analysis, writing – review and editing.

Acknowledgements

Project funded by the National Natural Science Foundation of China (52472297, 12305327), Natural Science Foundation of Jiangxi Province (20252BAC210010). Talent Project of Double Thousands Plan in Jiangxi Province (jxsq2020101056). Major Science and Technology Project of Jiangxi Province (20252ABG010006). The "2030 Sailing Plan" Basic Research Project of Jiangxi Province (20262BAC260013). We gratefully acknowledge HZWTECH for providing computation facilities. S.P. acknowledges the basic funding of the Helmholtz Association and the start-up funding of the International Electrochemical Energy Storage Research Institute (IEES), Nanjing Normal University (Grant No. 1840800014).

Open access funding enabled and organized by Projekt DEAL.

Conflicts of Interest

The authors declare no conflicts of interest.

Data Availability Statement

The data that support the findings of this study are available on request from the corresponding author. The data are not publicly available due to privacy or ethical restrictions.

References

1. J.-G. Zhang, W. Xu, J. Xiao, X. Cao, and J. Liu, "Lithium Metal Anodes With Nonaqueous Electrolytes," *Chemical Reviews* 120 (2020): 13312–13348.

2. D. Liu, B. Wu, Y. Xu, et al., "Controlled Large-Area Lithium Deposition to Reduce Swelling of High-Energy Lithium Metal Pouch Cells in Liquid Electrolytes," *Nature Energy* 9 (2024): 559–569.

3. J. Wang, H. Hyun, S. Seo, et al., "A Kinetic Indicator of Ultrafast Nickel-Rich Layered Oxide Cathodes," *ACS Energy Letters* 8 (2023): 2986–2995.

4. Y. Tang, X.-Y. Wang, J.-C. Ren, et al., "Insight Into Structural Degradation of NCMs Under Extreme Fast Charging Process," *Rare Metals* 43 (2024): 41–50.

5. J. Cai, X. Zhou, L. Li, et al., "Kinetically Dormant Ni-Rich Layered Cathode During High-Voltage Operation," *Advanced Materials* 37 (2025): 2419253.

6. X. Gao, Y. Chen, L. Johnson, and P. G. Bruce, "Promoting Solution Phase Discharge in Li–O_2 Batteries Containing Weakly Solvating Electrolyte Solutions," *Nature Materials* 15 (2016): 882–888.

7. X. Li, F. Luo, M. Yu, R. Liu, S. Zhao, and S. Fang, "Enhancing Lithium Metal Battery Performance With a Perfluorinated Bisalt Electrolyte Achieving High-Voltage Stability up to 4.8 V," *Energy Storage Materials* 75 (2025): 104048.

8. Y. Ou, C. Li, H. Zhou, et al., "Supramolecular Chemistry for High-Performance Lithium Metal Batteries," *CCS Chemistry*, 7, no. 10), (2025), 2864–2898, https://doi.org/10.31635/ccschem.025.202506033.

9. D. Larcher and J. M. Tarascon, "Towards Greener and More Sustainable Batteries for Electrical Energy Storage," *Nature Chemistry* 7 (2014): 19–29.

10. S. Zhao and F. Huang, "Weakly Solvating Few-Layer-Carbon Interface Toward High Initial Coulombic Efficiency And Cyclability Hard Carbon Anodes," *ACS Nano* 18 (2024): 1733.

11. X. Shi, J. Xie, J. Wang, S. Xie, Z. Yang, and X. Lu, "A Weakly Solvating Electrolyte Towards Practical Rechargeable Aqueous Zinc-Ion Batteries," *Nature Communications* 15 (2024): 302.

12. X. Li, F. Luo, N. Zhou, et al., "Weakly Solvating Electrolytes for Lithium and Post-Lithium Rechargeable Batteries: Progress and Outlook," *Advanced Energy Materials* 15 (2025): 2501272.

13. L. Suo, O. Borodin, T. Gao, et al., ""Water-In-Salt" Electrolyte Enables High-Voltage Aqueous Lithium-Ion Chemistries," *Science* 350 (2015): 938–943.

14. J. Wang, Y. Yamada, K. Sodeyama, C. H. Chiang, Y. Tateyama, and A. Yamada, "Superconcentrated Electrolytes for a High-Voltage Lithium-Ion Battery," *Nature Communications* 7 (2016): 12032.

15. S. Chen, J. Zheng, D. Mei, et al., "High-Voltage Lithium-Metal Batteries Enabled by Localized High-Concentration Electrolytes," *Advanced Materials* 30 (2018): 1706102.

16. X. Cao, X. Ren, L. Zou, et al., "Monolithic Solid–Electrolyte Interphases Formed in Fluorinated Orthoformate-Based Electrolytes Minimize Li Depletion and Pulverization," *Nature Energy* 4 (2019): 796–805.

17. Z. Wang and B. Zhang, "Weakly Solvating Electrolytes for Next-Generation Lithium Batteries: Design Principles and Recent Advances," *Energy Materials and Devices* 1 (2023): 9370003.

18. G. Zhang, T. Zhang, Z. Zhang, et al., "High-Energy and Fast-Charging Lithium Metal Batteries Enabled by Tuning Li^+-Solvation Via Electron-Withdrawing and Lithiophobicity Functionality," *Nature Communications* 16 (2025): 4722.

19. Y. Wen, Y. Liao, M. Xiao, et al., "Cooperative Trifluoromethyl Group and Catalyst-Enabled Regioselective 3,4-Functionalization of Unsymmetric β - CF 3 -1,3-Enynes via C–H Bond Activation," *Chinese Journal of Chemistry* 43 (2025): 2512–2518.

20. M. Adachi, K. Tanaka, and K. Sekai, "Aromatic Compounds as Redox Shuttle Additives for 4 V Class Secondary Lithium Batteries," *Journal of The Electrochemical Society* 146 (1999): 1256–1261.

21. S.-D. Han, J. L. Allen, E. Jónsson, et al., "Solvate Structures and Computational/Spectroscopic Characterization of Lithium Difluoro(oxalato)borate (LiDFOB) Electrolytes," *The Journal of Physical Chemistry C* 117 (2013): 5521–5531.

22. D. Lin-Vien, N. B. Colthup, W. G. Fateley, and J. G. Grasselli, *The Handbook of Infrared and Raman Characteristic Frequencies of Organic Molecules*, Academic Press, 1991.

23. Y. Yu, S. Wang, J. Zhang, et al., "Long-Life Lithium Batteries Enabled by a Pseudo-Oversaturated Electrolyte," *Carbon Energy* 6 (2023): 383.

24. W. Wahyudi, X. Guo, V. Ladelta, et al., "Hitherto Unknown Solvent and Anion Pairs in Solvation Structures Reveal New Insights Into High-Performance Lithium-Ion Batteries," *Advanced Science* 9 (2022): 2202405.

25. T. Ma, Y. Ni, Q. Wang, et al., "Optimize Lithium Deposition at Low Temperature by Weakly Solvating Power Solvent," *Angewandte Chemie International Edition* 61 (2022): 202207927.

26. Z. Wu, C. Zhang, F. Yuan, et al., "Ni-Rich Cathode Materials for Stable High-Energy Lithium-Ion Batteries," *Nano Energy* 126 (2024): 109620.

27. Y. Ou, W. Hou, D. Zhu, et al., "Molecular design of electrolyte additives for high-voltage fast-charging lithium metal batteries," *Energy &Amp; Environmental Science*, 18, no. 3, (2025) 1464–1476, https://doi.org/10.1039/d4ee04282d.

28. F. Cheng, W. Zhang, Q. Li, C. Fang, J. Han, and Y. Huang, "High Chaos Induced Multiple-Anion-Rich Solvation Structure Enabling Ultrahigh Voltage and Wide Temperature Lithium-Metal Batteries," *ACS Nano* 17 (2023): 24259–24267.

29. G. W. Nam, N.-Y. Park, K.-J. Park, et al., "Capacity Fading of Ni-Rich NCA Cathodes: Effect of Microcracking Extent," *ACS Energy Letters* 4 (2019): 2995–3001.

30. C. Xu, K. Märker, J. Lee, et al., "Bulk Fatigue Induced by Surface Reconstruction in Layered Ni-Rich Cathodes for Li-Ion Batteries," *Nature Materials* 20 (2021): 84–92.

31. H. Li, A. Liu, N. Zhang, et al., "An Unavoidable Challenge for Ni-Rich Positive Electrode Materials for Lithium-Ion Batteries," *Chemistry of Materials* 31 (2019): 7574–7583.

32. P. Yan, J. Zheng, T. Chen, et al., "Coupling of Electrochemically Triggered Thermal and Mechanical Effects to Aggravate Failure in a Layered Cathode," *Nature Communications* 9 (2018): 2437.

33. S. Liu, P. J. West, H. Zhong, et al., "Origin of Phase Separation in Ni-Rich Layered Oxide Cathode Materials During Electrochemical Cycling," *Chemistry of Materials* 35 (2023): 8857–8871.

34. H. Wang, D. Yan, H. Liu, et al., "A Non-Concentrated Gradient-Solvation Electrolyte Enables a High-Voltage Lithium Metal Battery With 447.6 Wh Kg^{-1}," *Advanced Materials* 37 (2025): 2509760.

35. B. Wang, K. Li, G. Xu, et al., "Mechanically and Chemically Co-Robust Ni-Rich Cathodes With Ultrahigh Capacity and Prolonged Cycle Life," *Angewandte Chemie International Edition* 64 (2025): 202502725.

36. Y. Zhang, Z. Yuan, B. Xie, et al., "Tailoring Anion-Enriched Solvation Structures in Phosphate-Based Electrolytes for Safety-Enhanced Lithium Metal Batteries," *Advanced Functional Materials* 35 (2025): 2504367.

37. Y. Xuerui, H. Yaxin, L. Jianhui, et al., "Understanding of working mechanism of lithium difluoro(oxalato) borate in Li||NCM85 battery with enhanced cyclic stability," *Energy Materials* 3 (2023): 300029.

38. W.-H. Hou, Y. Ou, T. Zeng, et al., "Rational molecular design of electrolyte additive endows stable cycling performance of cobalt-free 5 V-class lithium metal batteries," *Energy &Amp; Environmental Science*, 17, no. 21, (2025) 8325–8336, https://doi.org/10.1039/d4ee03280b.

39. Y. Wang, H. Zheng, L. Hong, et al., "Lithium Difluoro(Bisoxalato) Phosphate-Based Multi-Salt Low Concentration Electrolytes for Wide-Temperature Lithium Metal Batteries: Experiments and Theoretical Calculations," *Chemical Engineering Journal* 445 (2022): 136802.

40. E. Yoo and H. Zhou, "Enhanced Cycle Stability of Rechargeable Li–O_2 Batteries by the Synergy Effect of a LiF Protective Layer on the Li and DMTFA Additive," *ACS Applied Materials & Interfaces* 9 (2017): 21307–21313.

41. X. Fan, X. Ji, F. Han, et al., "Fluorinated Solid Electrolyte Interphase Enables Highly Reversible Solid-State Li Metal Battery," *Science Advances* 4 (2018): aau9245.

Supporting Information

Additional supporting information can be found online in the Supporting Information section.

Supporting File: aenm71380-sup-0001-SuppMat.docx.